Chemistry–A European Journal
Research Article
doi.org/10.1002/chem.202302832
Chemistry Europe
European Chemical Societies Publishing
www.chemeurj.org

Mechanism of CO_2 Reduction to Methanol with H_2 on an Iron(II)-scorpionate Catalyst

Chengxu Zhu,[a, b] Carmine D'Agostino,[b, c] and Sam P. de Visser*[a, b]

CO_2 utilization is an important process in the chemical industry with great environmental power. In this work we show how CO_2 and H_2 can be reacted to form methanol on an iron(II) center and highlight the bottlenecks for the reaction and what structural features of the catalyst are essential for efficient turnover. The calculations predict the reactions to proceed through three successive reaction cycles that start with heterolytic cleavage of H_2 followed by sequential hydride and proton transfer processes. The H_2 splitting process is an endergonic process and hence high pressures will be needed to overcome this step and trigger the hydrogenation reaction. Moreover, H_2 cleavage into a hydride and proton requires a metal to bind hydride and a nearby source to bind the proton, such as an amide or pyrazolyl group, which the scorpionate ligand used here facilitates. As such the computations highlight the non-innocence of the ligand scaffold through proton shuttle from H_2 to substrate as an important step in the reaction mechanism.

Introduction

Carbon dioxide is one of the main chemicals contributing to global warming and its concentration in the atmosphere has been steadily increasing since the Industrial Revolution. In recent years, therefore, research has focused on carbon dioxide utilization and its chemical conversion into valuable materials, such as hydrocarbons, esters, alcohols etc.[1] Thus, Nature utilizes several enzymes for CO_2 reduction processes particularly in plants and bacteria.[2] Moreover, a number of homogeneous catalysts have been designed for CO_2 reduction processes at room temperature with either porphyrinoid or nonheme ligands environments.[3] In particular, iron-porphyrinoid complexes with groups on the second coordination sphere that can assist with proton relay mechanisms were shown to be very efficient for electrochemical CO_2 to CO reduction processes.[4] These studies trapped and characterized short-lived intermediates and measured electrochemical reduction processes. Density functional theory studies on the CO_2 to CO reduction on iron-porphyrin systems showed the electronic features during the reaction processes and the proton transfer delivery.[5] Furthermore, an iron(I)-porphyrin system with variable *meso*-substituents was shown to give competitive reduction of CO_2 to either CO or methane under a H_2 atmosphere and reaction conditions were explored to improve the selectivity.[6]

By contrast, homogeneous iron catalysts for CO_2 reduction at room temperature are rare. Montandon-Clerc and Laurenczy reported an iron(II) complex with *meta*-trisulfonated-tris[2-(diphenylphosphino)ethyl]phosphine ligand that in the presence of 75 atm of H_2 and CO_2 gas reacted to form formic acid products.[7] Using an iron(II)-pincer complex the reaction of H_2 and CO_2 gas was studied in the presence of amide.[8] The authors established a mechanism that started with the H_2 cleavage on iron, followed by the formation of a formamide, which subsequently reacts to give methanol products in another reaction with H_2. Similar reactivity was observed on a manganese(I)-pincer complex that also produced methanol from CO_2 and H_2 gas.[9] Pombeiro and co-workers[10] reported a novel iron(II)-scorpionate ligand system, namely with the hydrotris(1-pyrazolyl)methane (κ^3-HC(pz)$_3$) tripodal metal coordination (Scheme 1) that under high pressure conditions at 80 °C was shown to convert CO_2 and H_2 to methanol efficiently with 44% yield. Under relatively mild conditions and even

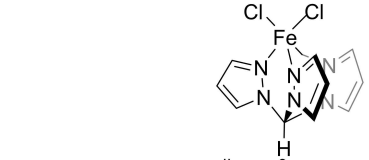

$CO_2 + 3\ H_2 \xrightarrow[80\ °C,\ 75\ atm,\ 24\ h,\ amine]{[Fe^{II}Cl_2(\kappa^3\text{-}HC(pz)_3)]} CH_3OH + H_2O$

Scheme 1. CO_2 reduction to methanol on an iron(II)-scorpionate catalyst as reported in ref. [10].

[a] C. Zhu, Dr. S. P. de Visser
Manchester Institute of Biotechnology
The University of Manchester
131 Princess Street, Manchester M1 7DN (United Kingdom)
E-mail: sam.devisser@manchester.ac.uk
[b] C. Zhu, Dr. C. D'Agostino, Dr. S. P. de Visser
Department of Chemical Engineering
The University of Manchester
Oxford Road, Manchester M13 9PL (United Kingdom)
Homepage: https://research.manchester.ac.uk/en/persons/sam.devisser
[c] Dr. C. D'Agostino
Dipartimento di Ingegneria Civile, Chimica, Ambientale e dei Materiali (DICAM), Alma Mater Studiorum
Università di Bologna
Via Terracini, 28, 40131 Bologna (Italy)

Supporting information for this article is available on the WWW under https://doi.org/10.1002/chem.202302832

under the absence of solvent and amine the reaction was shown to proceed. A combination of experimental and computational approaches investigated the $[Fe^{II}Cl_2(\kappa^3\text{-}HC(pz)_3]$ system and identified spectroscopic and electronic features of the catalyst.[11] To understand the details of the CO_2 conversion to methanol on this iron(II)-scorpionate ligand system we decided to do a detailed density functional theory study into possible mechanisms for CO_2 reduction and obtain insight into the function and properties of the metal and ligand system.

Computational studies can give insight into fast reaction processes that are difficult to trap experimentally and consequently can establish rate-determining steps in reaction mechanisms, the nature of an active oxidant or reductant as well as electronic information on what drives the reaction processes.[12] These insights can assist with further development and design of catalysts. Several computational studies have been reported on CO_2 reduction on iron and manganese catalysts.[5,13] In particular, these studies show that CO_2 binding is slightly endergonic and consequently may determine the rate, while the reduction and proton abstraction steps appear to be exergonic. Here we report a computational study on $[Fe^{II}(\kappa^3\text{-}HC(pz)_3)]$ and show that CO_2 reduction with H_2 gives methanol rather than CO products as the available hydride and protons enable efficient transfer to the iron-bound substrate. In particular, the reaction is initiated by heterolytic cleavage of H_2 into a hydride that binds to iron and a proton that binds to a pyrazolyl group of the ligand scaffold. These studies highlight the non-innocence and importance of the ligand in the reaction mechanism.

Results and Discussion

Binding of H_2 and CO_2 to the iron(II)-scorpionate complex

In principle, the reaction described in Scheme 1 starts with an $[Fe(Cl_2)(\kappa^3\text{-}HC(pz)_3)]$ complex and replacement of the chlorine ions with substrates. We calculated the $[Fe(Cl_2)(\kappa^3\text{-}HC(pz)_3)]$, $[Fe(Cl)(\kappa^3\text{-}HC(pz)_3)]^+$ and $[Fe(\kappa^3\text{-}HC(pz)_3)]^{2+}$ complexes in the quintet spin state as well as an isolated Cl^- ion and determined the halide binding energies to the complexes. We calculate a free energy for release of one halide ion of $\Delta G = 11.6$ kcal mol^{-1} and a value of $\Delta G = 25.5$ kcal mol^{-1} for the removal of a second halide ion. As such the halide ions are weakly bound to the complex and will split off rapidly in solution or in the presence of amine molecules in the chemical system.

Next, the possible binding of CO_2 and H_2 to the iron(II)-scorpionate complex was studied. To this end, we created models of $[Fe^{II}(\kappa^3\text{-}HC(pz)_3)]^{2+}$ and added one or more H_2 and CO_2 molecules to the complex. Thus, in model **A** we included one H_2 and one CO_2 molecule bound to iron, whereas model $\mathbf{A}_{3CO2}$ contains the iron(II)-scorpionate with one H_2 and three CO_2 molecules while in model $\mathbf{A}_{3H2}$ the iron(II)-scorpionate is surrounded by three H_2 molecules and one CO_2 molecule. Subsequently, full geometry optimizations of these three complexes in the lowest energy singlet, triplet and quintet spin states were performed. We identify the spin state with a superscript in front of the label.

The optimized geometries of the complexes **A**, $\mathbf{A}_{3CO2}$ and $\mathbf{A}_{3H2}$ are shown in Figure 1. The quintet spin state is the ground state for all complexes by more than $\Delta G = 20$ kcal mol^{-1}. In particular, ^{3}**A** and ^{1}**A** are higher in free energy than the quintet spin state by $\Delta G = 20.7$ and 23.1 kcal mol^{-1}, respectively. As can be seen in all complexes CO_2 binds to iron with an Fe–O bond of 2.252–2.266 Å in the quintet spin state structures. This is a typical distance for the interaction of a neutral ligand to iron and, for instance, seen for the interaction of a histidine to iron in protein structures,[14] but also in previous studies on CO_2 binding to homogeneous iron catalysts as well as biomimetic model complexes.[5,15] The H_2 molecule binds side-on with the Fe–H bonds of similar length. In the triplet spin state it is stronger bound with much shorter Fe–H distances than in the quintet spin state, where they are 2.124/2.182 Å in ^{5}**A** and 2.247/2.249 Å in $^5\mathbf{A}_{3H2}$. Interestingly, when multiple CO_2 molecules are in the model as in $^5\mathbf{A}_{3CO2}$, then H_2 binding is weakened and the nearest Fe–H distance is 3.124 Å. A structure with excess CO_2, therefore, may not give hydrogenation of CO_2 and more efficient catalysis will be obtained with access H_2. Indeed the experimental work of Pombeiro et al.[10] used a 3:1 ratio of the pressures of H_2 and CO_2 in support of the models described in Figure 1.

To find possible reaction mechanisms of CO_2 reduction to methanol we continued with the model with one CO_2 and H_2 molecule bound to iron and after the hydrogenation added the second H_2 molecule, while the third H_2 molecule was added after the second hydrogenation step was completed.

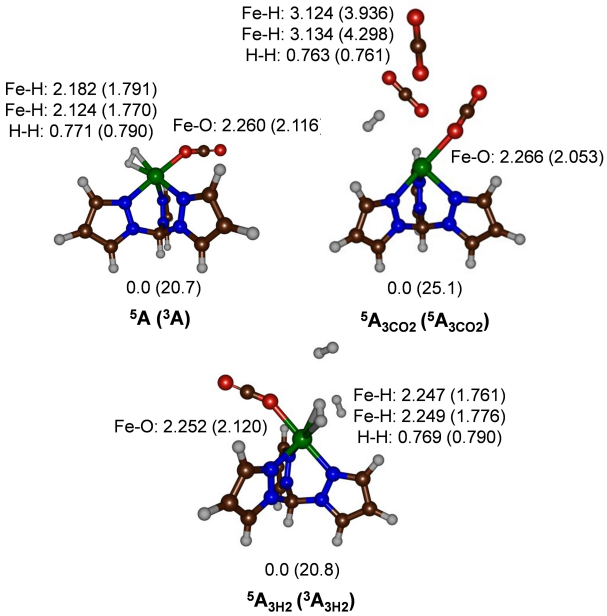

Figure 1. UB3LYP-GD3/BS1 optimized geometries of CO_2 and H_2 bound iron(II)-scorpionate complexes. Bond lengths are in angstroms.

First hydrogenation step of CO_2 by H_2

Subsequently, three consecutive reaction cycles were explored for the H_2 addition to CO_2 on the iron(II)-scorpionate center to form methanol products. The work started from the iron(II)-scorpionate complex containing one H_2 and one CO_2 molecule (Model **A**) and in reaction cycle 1 (Scheme 2) focused on the hydrogenation of CO_2 to form formic acid products. For reaction cycle 1, we considered the initial H_2 cleavage to form **IM1a** via transition state **TS1a** and the subsequent hydride transfer to the carbon atom of CO_2 to form formate (via transition state **TS2a** to give **IM2a**). Structure **IM2a** would be an iron(III)-formate bound complex that can pick up a proton to form formic acid products **IM3a** via transition state **TS3a**. In addition, we considered direct attack of bound and free H_2 to the oxygen atom of CO_2 in the reactant-bound structure ^{5,3}**A** to form **IM1b** via **TS1b** and attack of H_2 on the carbon atom of CO_2 to give **IM1c** via **TS1c**, while in all these cases the hydride remains attached to iron. For the protonated CO_2-bound structure **IM1b** we also considered a mechanism for formic acid bound iron(II) products formation **IM3a** via transition state **TS2b** or alternatively a pathway for addition of another proton to the protonated carbon dioxide species through the formation of CO and water (**IM2b** via **TS2d**). The internal proton transfer from the Fe–H group in **IM1c** to formate will give **IM3a** via **TS2c**. All mechanisms and pathways were calculated with DFT on the lowest energy quintet and triplet spin state surfaces, see Supporting Information for details.

The lowest energy pathway for the first hydrogenation step of CO_2 by H_2 on the iron(II)-scorpionate complex is shown in Figure 2. Although we tested direct attack of H_2 on CO_2 either on the iron center or as unbound molecules *via* **TS1b** or **TS1c**, this did not give any low energy pathways, see Supporting Information for details. Consequently, direct attack is unfeasible and a metal catalyst is needed to guide the CO_2 hydrogenation reaction. Indeed, an initial step for dihydrogen bond cleavage via ^{5}**TS1a** is found to trigger the hydrogenation reaction, whereby the hydride remains bound to iron and the proton is transferred to one of the pyrazolyl nitrogen atoms, which then loses its bond to iron. A free energy of activation of $\Delta G^{\ddagger} = 19.6\ \mathrm{kcal\,mol^{-1}}$ is calculated for dihydrogen bond cleavage. However, the local minimum with the proton attached to nitrogen and the hydride bound to iron is endergonic with respect to reactants by $\Delta G = 17.5\ \mathrm{kcal\,mol^{-1}}$. Therefore, it is likely that the reverse reaction from the transition state will dominate and make the reaction inefficient. Not surprisingly, experimental work showed the reaction only to proceed under high pressure conditions of 75 atm,[10] which is consistent with an endergonic initial reaction step for dihydrogen cleavage. These high pressures, therefore, will push the reaction process further and enable the next reaction step for heterolytic cleavage of the H_2 bond to proceed. The dihydrogen bond cleavage transition state ^{5}**TS1a** is shown in Figure 2. It has a large imaginary frequency of $i1071\ \mathrm{cm^{-1}}$ for the H–H stretch vibration. This large value implicates the reaction is likely to proceed with a considerable amount of quantum chemical tunneling and particularly will be affected by hydrogen by

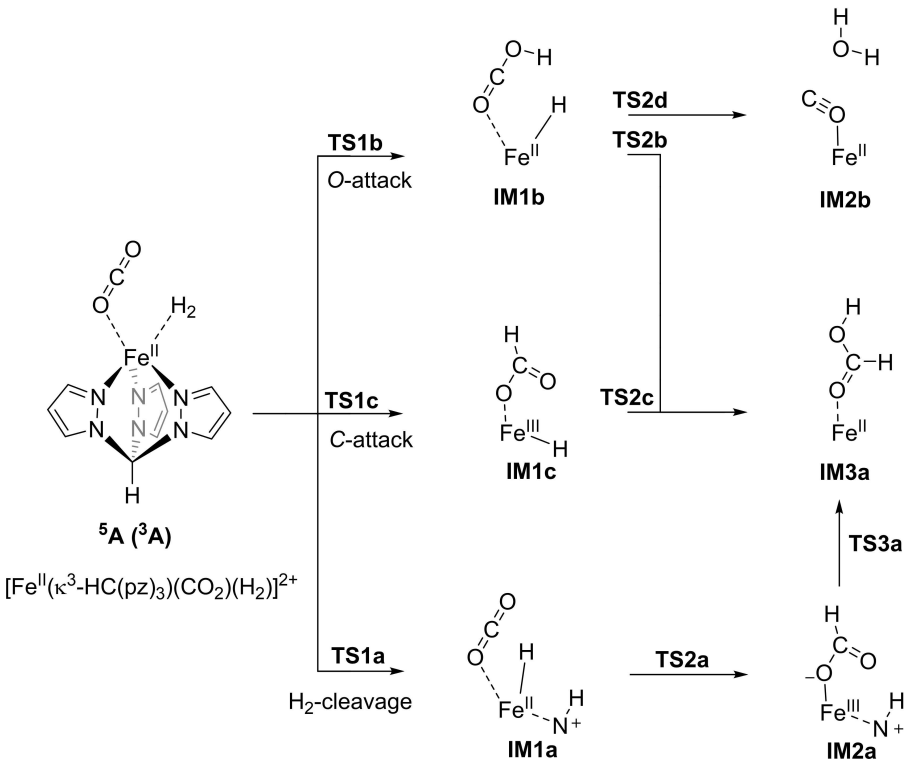

Scheme 2. Catalytic mechanism with definitions of transition states and local minima as calculated for the first reduction of CO_2 on $[Fe^{II}(\kappa^3\text{-}HC(cz)_3]^{2+}$ upon addition of one molecule of H_2.

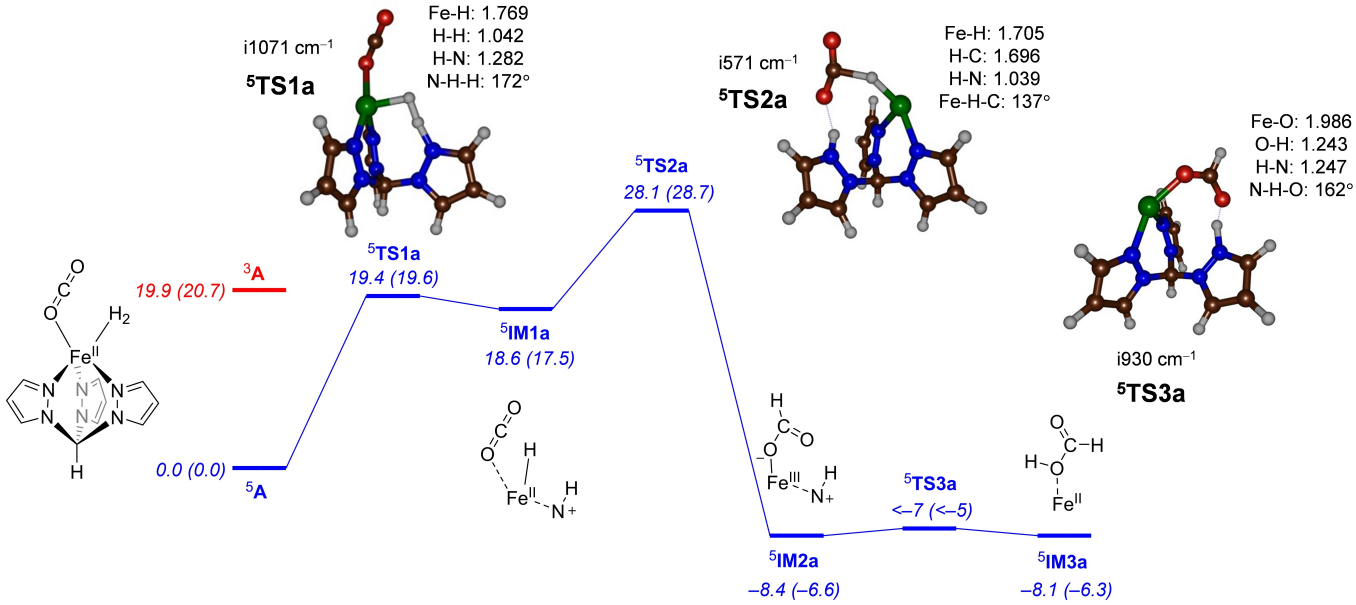

Figure 2. UB3LYP-GD3/BS2//UB3LYP-GD3/BS1 calculated potential energy profile for the first hydrogenation step of CO_2 by an iron(II)-scorpionate complex. Outside parenthesis are ΔE + ZPE energies (in kcal mol^{-1}) while free energy differences calculated at 298 K are in parenthesis. Transition state structures are shown with bond lengths in Å, bond angles in degrees and the imaginary frequency in cm^{-1}.

deuterium substitution leading to a kinetic isotope effect.[16] The dihydrogen bond has weakened in the transition state to 1.042 Å, while the N–H distance is shortened to 1.282 Å. Also the Fe–H bond has considerably shortened from 2.124 Å in ^{5}**A** to 1.769 Å in ^{5}**TS1a**. The N–H–H angle is almost linear in the transition state at 172°. After dihydrogen cleavage, a hydride transfer from the iron atom to the carbon atom of CO_2 takes place via transition state ^{5}**TS2a**. Its barrier is significant and located at $\Delta G^{\ddagger} = 28.7$ kcal mol^{-1}, which makes it the rate determining step in the first hydrogenation cycle of CO_2. The transition state has an imaginary frequency of i571 cm^{-1}, which is a low value for a hydride transfer step, but its animation gives a clear C–H–Fe stretch vibration. Most likely the low value is due to the significant bending of the Fe–H–C interaction (137°), probably due to the hydrogen bonding interaction of one of the oxygen atoms of CO_2 with the proton on the pyrazolyl group. Interestingly, the Fe–H distance has not changed significantly from ^{5}**IM1a** to ^{5}**TS2a** (1.703 vs 1.705 Å, respectively); consequently, the transition state is early on the potential energy surface and is closer in resemblance to reactants than products. The formate-bound iron(III) complex ^{5}**IM2a** is lower in free energy than the reactants complex by $\Delta G = -6.6$ kcal mol^{-1}. It forms a strong hydrogen bonding interaction through one of its oxygen atoms with the proton on the pyrazolyl group. A negligible barrier of less than 1 kcal mol^{-1} above ^{5}**IM2a** leads to the formic acid bound product structure ^{5}**IM3a**, which is of similar energy as ^{5}**IM2a** hence the two structures will be in equilibrium. We managed to characterize ^{5}**TS3a** and it has a large imaginary frequency of i930 cm^{-1} for proton transfer. Structurally, in ^{5}**TS3a** the transferring proton is midway between the donor nitrogen atom and accepting oxygen atom: H–O and H–N distances of 1.243 and 1.247 Å are found.

We also attempted mechanisms for direct H_2 attack on CO_2 in the reactant complexes, see Supporting Information. On the triplet spin state both of these transition states (^{3}**TS1b** and ^{3}**TS1c**) were characterized and found to be >40 kcal mol^{-1} higher in energy than ^{3}**TS1a**. Geometry scans on the quintet spin state for the direct attack pathway of H_2 on either the carbon atom or the oxygen atom of CO_2 gave a similar result with high energy barriers. Therefore, a direct H_2 pathway for CO_2 hydrogenation is not a feasible mechanism. Instead the reaction will take place through binding of H_2 to the iron center and an initial H_2 heterolytic cleavage mechanism that gives a hydride bound to iron and a protonated pyrazolyl group. Consequently, the CO_2 hydrogenation to form formic acid products happens through consecutive hydride followed by proton transfer steps.

Second hydrogenation step by H_2

After the initial hydrogenation cycle of CO_2, we took the formic acid-bound iron(II) structure (**IM3a**) and added another H_2 molecule to form structure **B** and proceeded the reaction mechanism for the next hydrogenation step as described in Scheme 3. In particular, we studied the reaction cycle to form either formaldehyde and water or methanediol. For reaction cycle 2 we considered dihydrogen bond cleavage via transition state **TS4** to form **IM4**. Thereafter, either a hydride is transferred to the carbon atom of formic acid (*via* **TS5a** to form **IM5a**) or to the carbonyl group of formic acid (*via* **TS5b** to form **IM5b**). Both intermediates can react with the remaining proton to form the methanediol intermediate **IM6a**. An alternative pathway considered was proton transfer to the alcohol group in **IM5a** to form water and formaldehyde products **IM6c** via transition state

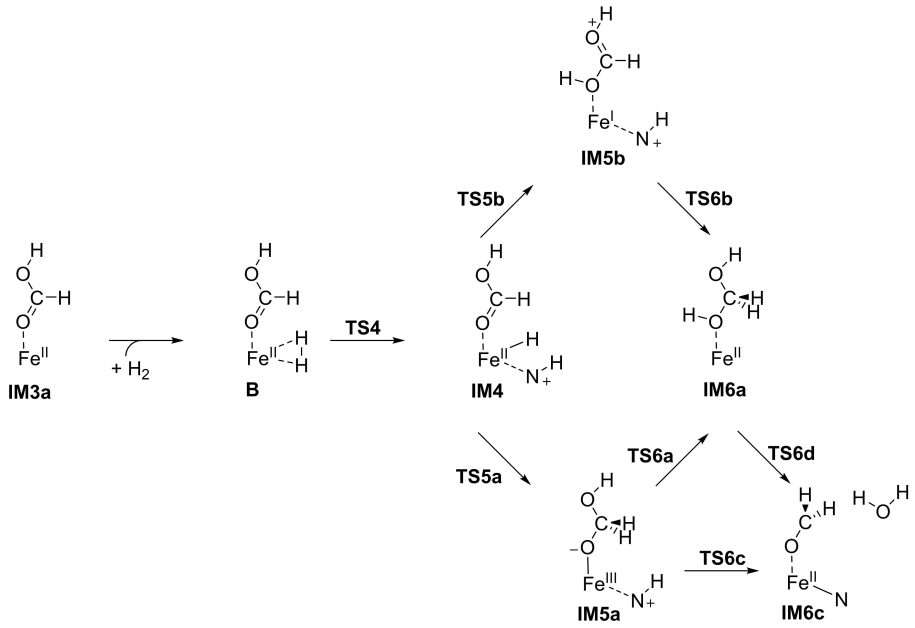

Scheme 3. Catalytic mechanism with definitions of transition states and local minima as calculated for the second reduction of CO_2 on $[Fe^{II}(\kappa^3\text{-}HC(cz)_3]^{2+}$ upon addition of a second molecule of H_2.

TS6c. This intermediate can also be reached from proton shuttle between the two OH groups in the diol structure **IM6a** *via* transition state **TS6d**.

Thus, to calculate cycle 2 of the process, we took the optimized geometry of ^{5}**IM3a** and added another H_2 molecule to the complex to form ^{5,3}**B** and did a full geometry optimization on the mechanism for hydrogenation of formic acid and the results are shown in Figure 3. Dihydrogen cleavage in ^{5}**B** requires a free energy of activation of $\Delta G^{\ddagger} =$ 22.2 kcal mol^{-1}, which is slightly higher in energy as the H–H cleavage barrier in cycle 1. At ΔE level of theory the barrier ^{5}**TS4** is higher in energy than the subsequent intermediate ^{5}**IM4** by 1.6 kcal mol^{-1}; however, addition of zero-point corrections reverses the energy gap and brings it slightly below the energy of the intermediate, which is caused by the removal of a high-energy C–H vibration in the transition state frequency. Nevertheless, the calculations imply a shallow saddle point for ^{5}**IM4** that is set-up for subsequent hydride transfer. The optimized geometry of transition state **TS4a** is very similar to **TS1a** with an imaginary frequency of i1035 cm^{-1} and an H–H distance of 1.057 Å. The H_2 molecule is at a distance of 1.767 Å from the iron atom and 1.265 Å from the proton acceptor from the

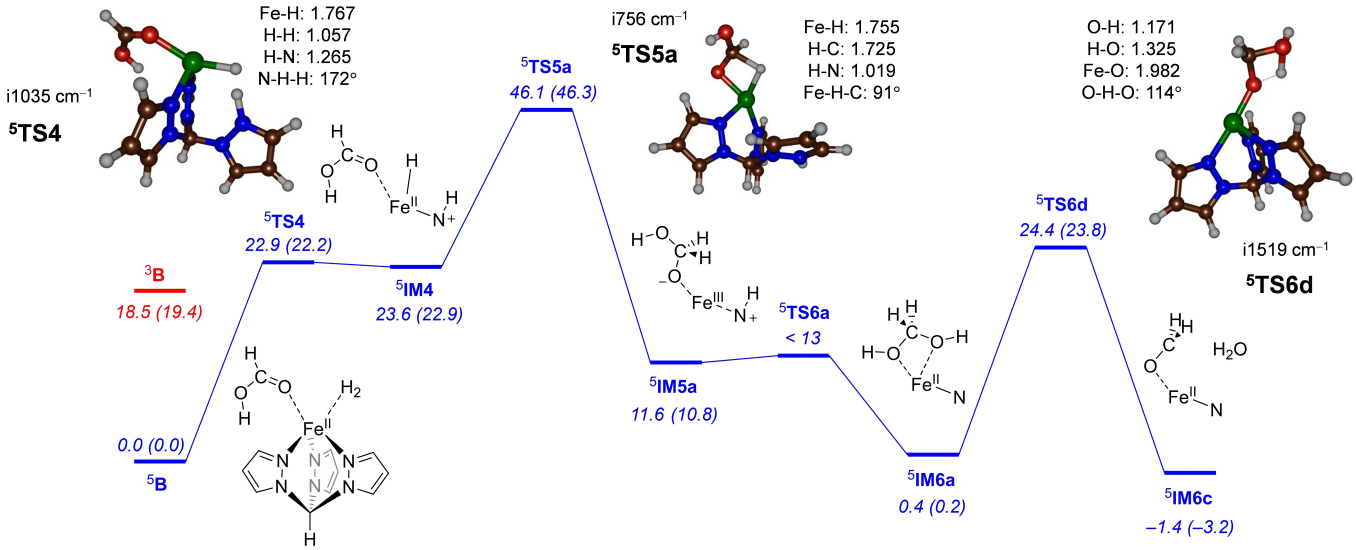

Figure 3. UB3LYP-GD3/BS2//UB3LYP-GD3/BS1 calculated potential energy profile for the second hydrogenation step of CO_2 by an iron(II)-scorpionate complex. Outside parenthesis are $\Delta E + ZPE$ energies (in kcal mol^{-1}) while free energy differences calculated at 298 K are in parenthesis. Transition state structures are shown with bond lengths in Å, bond angles in degrees and the imaginary frequency in cm^{-1}.

pyrazolyl group. From ^{5}**IM4a** a hydride transfer takes place to give ^{5}**IM5a**. The barrier for this step is considerably higher in free energy than the hydride transfer in cycle 1 (at $\Delta G^{\ddagger} =$ 46.3 kcal mol^{-1}) and consequently requires high pressure and high concentration and elevated temperatures to proceed. Structure ^{5}**TS5a** has a large imaginary frequency typical for H-transfer processes with a magnitude of i756 cm^{-1}. The hydride is located midway in between the donor and acceptor atoms, i.e. the Fe–H distance is 1.755 Å and the C–H distance is 1.725 Å, while the angle for the Fe–H–C interaction is strongly bent at 91°. The small angle may be the origin for the large energetic barrier for this step. Typical hydrogen transfer barriers have a linear orientation between the donor and acceptor groups with a typical angle close to 180°.[17]

Next, two pathways for proton transfer were tested, namely proton transfer to the hydroxo group to form water or proton transfer to the oxo group to form methanediol. The latter barrier was low in energy and a geometry scan located it at $<$1.3 kcal mol^{-1} above ^{5}**IM5a**, Supporting Information Figure S6. Unfortunately, we failed to characterize a transition state for this step, but it is clear the proton transfer to form methanediol is low in energy. The alternative pathway via ^{5}**TS6c** was also explored; however, during the geometry scan from ^{5}**IM5a** for proton transfer to the hydroxo group, the proton moved to the oxo group and ^{5}**IM6a** was formed instead. Consequently, the pathway via ^{5}**TS6c** is unfeasible. We did, however, characterize ^{5}**TS6d** for the intramolecular proton transfer in methanediol to form water and formaldehyde, see Figure 3. This transition state is $\Delta G^{\ddagger} = 23.8$ kcal mol^{-1} higher in energy than ^{5}**B** and leads to ^{5}**IM6c**. Structurally, ^{5}**TS6d** has a large imaginary frequency of i1519 cm^{-1} characteristic for proton transfer. The transferring proton is closer to the donor oxygen atom than the acceptor group: 1.171 versus 1.325 Å.

In summary, the second reaction cycle has a rate-determining hydride transfer reaction of high energy that will require high pressures and temperatures. Thereafter, proton transfer can happen to give either the diol or formaldehyde intermediates. As these two intermediates may both be stable, we continued the final reaction cycle from both intermediates by adding another hydrogen molecule to the structure to get structures **C** and **D**.

Third hydrogenation step by H_2

For the final reaction cycle for the third hydrogenation step of CO_2, we took the methanediol-bound iron(II) structure **IM6a** and the formaldehyde-bound iron(II) structure **IM6c** and added another H_2 molecule to give the structures **C** and **D**, respectively. A final reaction cycle with another H_2 molecule added then focused on the generation of methanol final products, see Scheme 4. Similarly to the second cycle, we calculated H_2 cleavage *via* **TS7a**/**TS7b** to form structures **IM7a**/**IM7b**. Both of these intermediates can react through hydride transfer to the carbon atom to form **IM8a** and **IM8b**, although the former may release the methanol group. In the final step either the OH^- in **IM8a** is protonated to form water and methanol products **IM9a** *via* **TS9a** or from **IM8b** the protonation of the methoxy group takes place *via* **TS9b** gives **IM9b**.

Subsequently, the final hydrogenation cycle was calculated starting from structures **C** and **D** and the potential energy landscape is shown in Figure 4. Structure **C** binds H_2 in a side-on fashion and leads to heterolytic cleavage of H_2 through a barrier ^{5}**TS7a** to form ^{5}**IM7a**. The transition states (^{5}**TS7a** and ^{5}**TS7b**) are both on a cusp close in free energy to their subsequent intermediates (**IM7a** and **IM7b**) and even though

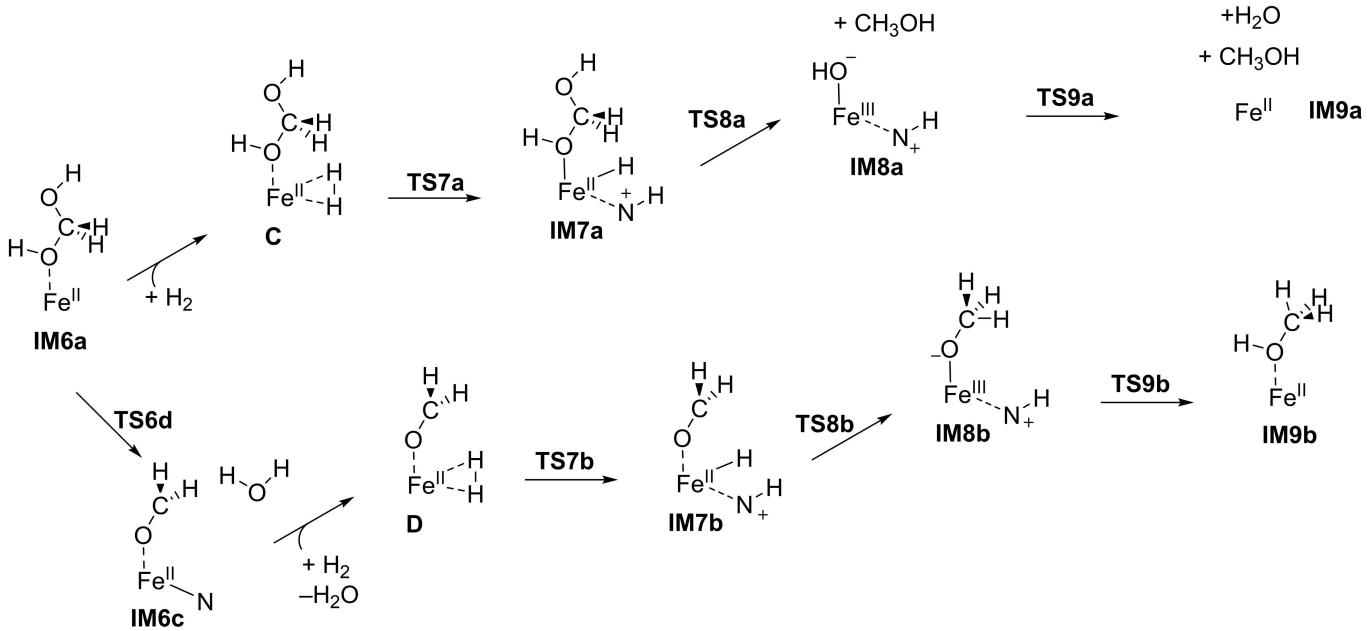

Scheme 4. Catalytic mechanism with definitions of transition states and local minima as calculated for the third reduction of CO_2 on $[Fe^{II}(\kappa^3\text{-}HC(cz)_3]^{2+}$ upon addition of a third molecule of H_2.

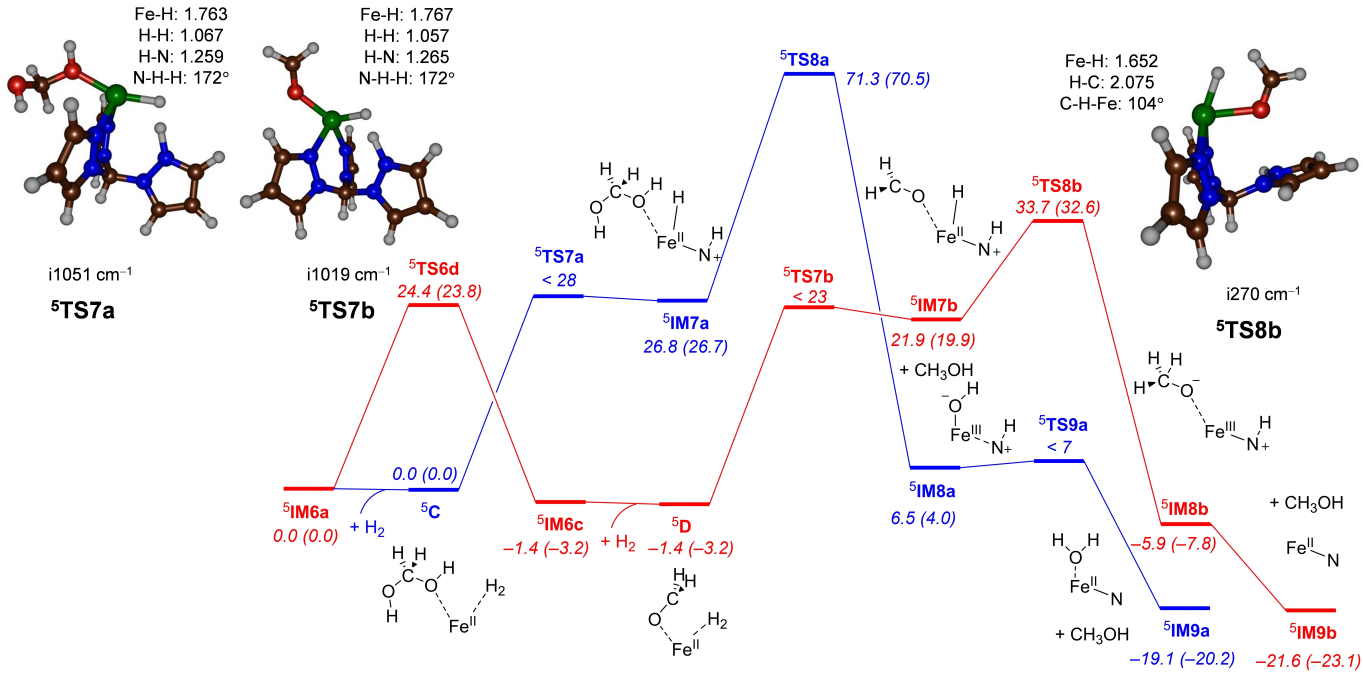

Figure 4. UB3LYP-GD3/BS2//UB3LYP-GD3/BS1 calculated potential energy profile for the third hydrogenation step of CO_2 by an iron(II)-scorpionate complex. Outside parenthesis are ΔE + ZPE energies (in kcal mol^{-1}) while free energy differences calculated at 298 K are in parenthesis. Key transition state structures are shown with bond lengths in Å, bond angles in degrees and the imaginary frequency in cm^{-1}.

they are higher in energy than ^{5}**IM7a**/^{5}**IM7b** at ΔE level of theory, they become degenerate after zero-point and thermal corrections are included, hence are labelled as <28 and <23 kcal mol^{-1} in Figure 4. Geometrically, the structure of ^{5}**TS7a** resembles ^{5}**TS1a** and ^{5}**TS4** with the H_2 bond elongated to 1.067 Å and Fe–H and N–H distances of 1.763 and 1.259 Å, respectively. The N–H–H angle is close to linearity at 172° and a large imaginary frequency for the H–H stretch vibration of i1051 cm^{-1} is obtained. This structure is similar to ^{5}**TS7b** that has Fe–H and N–H distances of 1.767 and 1.265 Å, respectively, while an imaginary frequency of i1019 cm^{-1} is obtained. The pathway starting from ^{5}**C** is then followed by a hydride transfer step via ^{5}**TS8a**, which was located at a free energy of $\Delta G^{\ddagger} =$ 70.5 kcal mol^{-1}. This is an exceptionally high free energy, which at room temperature will unlikely make the process possible. Consequently, the pathway via ^{5}**C** is a dead-end reaction channel and will not lead to methanol products and stop at the methanediol products.

As discussed above in Figure 3 the methanediol complex ^{5}**C** through internal proton transfer can split off water and form formaldehyde complex ^{5}**IM6c** that after binding H_2 gives complex ^{5}**D**. We then followed the hydrogenation of formaldehyde from ^{5}**D**. This system has a much lower free energy for hydride transfer via ^{5}**TS8b** of $\Delta G^{\ddagger} = 32.6$ kcal mol^{-1} above ^{5}**D**. The transition state structure is shown in Figure 4 and has an imaginary frequency of i270 cm^{-1} for the C–H–Fe stretch vibration. The distances in the transition state are 1.652 Å for the Fe–H bond and 2.075 Å for the C–H bond. After the hydride transfer the system relaxes to methanolate-bound iron(III) with large exothermicity. A final barrierless proton transfer then gives final methanol products.

Overall reaction pathway established from DFT calculations

The calculations described in this work focus on CO_2 reduction to methanol with three molecules of H_2 on a nonheme iron(II)-scorpionate complex. The work has established a mechanism with three successive reaction cycles for H_2 binding and addition to substrate as described and summarized in Scheme 5. Calculations with multiple CO_2 and H_2 molecules nearby iron(II) show that excess H_2 is needed to enable direct binding of H_2 to the metal center as it binds weaker than CO_2 and will not be able to compete with it. Upon H_2 binding each reaction cycle starts with heterolytic cleavage of H_2 into a hydride and a proton, whereby the metal binds the hydride and one of the pyrazolyl rings binds the proton. The H_2-cleavage barriers in cycle 1, 2 and 3 have similar free energies of activation and lead to an endergonic reaction step for the formation of the cleaved H_2-molecule complex. Therefore, high pressures will be needed to overcome this initial endergonic step in the reaction mechanism and enable the CO_2 hydrogenation reactions. The H_2-cleavage barrier is not rate-determining but the subsequent hydride transfer from iron to substrate, which has barriers of $\Delta G^{\ddagger} = 28.7$, 46.3 and 32.6 kcal mol^{-1} for cycles 1, 2, and 3, respectively. The free energy of activation of the second cycle is relatively high and therefore will require considerably high pressures and temperatures to proceed. Moreover, significant amount of acetic acid should be observed after completion of the first cycle. After the hydride is transferred a facile proton transfer completes each cycle. In all three cycles the proton transfer step is fast and rapidly takes place to form the products of each reaction cycle. In summary, in cycle 1 the CO_2 is reduced to formic acid, in cycle 2 the formic acid is

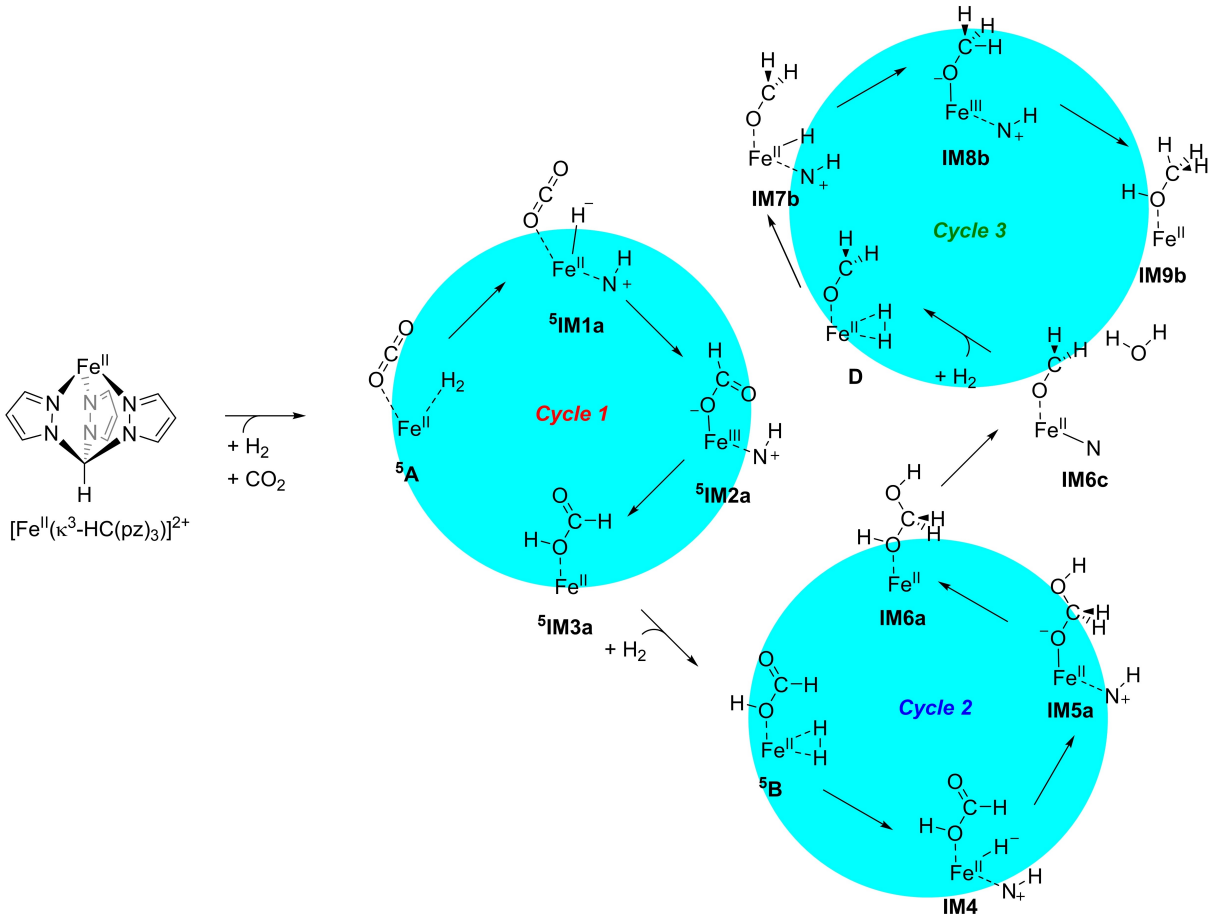

Scheme 5. Reaction mechanism of CO_2 reduction by H_2 on an iron(II)-scorpionate system as established from this work.

reduced to formaldehyde and water via a methanediol intermediate, while in the final cycle formaldehyde is reduced to methanol. As some barriers, particularly those for hydride transfer are relatively high in free energy, it may be possible to trap formic acid and formaldehyde intermediates experimentally.

The mechanisms for CO_2 reduction to methanol shown in Scheme 5 highlight some important features for catalyst development and design. Firstly, an environmentally benign CO_2 reduction process that utilizes H_2 is energetically demanding as H_2 will need to be cleaved heterolytically and bind to the catalyst center as individual hydride and proton. Therefore, a transition metal is needed to bind the hydride. Generally, heavy metals ions bind a hydride relatively easily and hence are commonly employed for CO_2 reduction processes. However, as shown here, a hydride can bind to iron as well, but in our system, it requires a lot of energy to form the hydride-bound complex from H_2 and iron(II) and consequently is energetically demanding. Secondly, the work described here highlights that CO_2 reduction by H_2 will need a proton acceptor in the vicinity of the catalyst complex and ideally the proton acceptor is bound to the metal center. The scorpionate ligand has several pyrrole groups that can bind and hold a proton for proton shuttle processes. Upon heterolytic cleavage of H_2 one of the iron-pyrazolyl bonds breaks and it picks up the proton instead and thereby facilitates proton transfer within the reaction complex efficiently. The pyrazolyl ligand that picks up the proton of H_2 loses its bond with iron and twists away from the metal center. However, it is close enough to the substrate so that an internal proton transfer is facilitated in the later stage of the reaction. As such, the iron(II)-scorpionate complex provides an ideal scaffold for hydrogenation of CO_2 by H_2 by enabling H_2 cleavage, proton and hydride storage and thereafter bringing all components together for efficient hydrogenation.

Orbital analysis of the reaction mechanism

To understand the origin of the catalytic mechanism and the features that drive the reaction, we analyzed the unpaired spin densities and orbital occupations of key local minima along the reaction mechanism. Figure 5 shows a valence bond description of the bond-forming and bond-breaking processes that happen in the initial cycle for first hydrogenation of CO_2 by a molecule of H_2 on the iron(II)-scorpionate complex. These schemes were used previously to rationalize regio- and chemoselectivities in reaction processes.[18] Thus, complex ^{5}**A** has four unpaired electrons located on the metal (spin of 3.84) in 3d-type

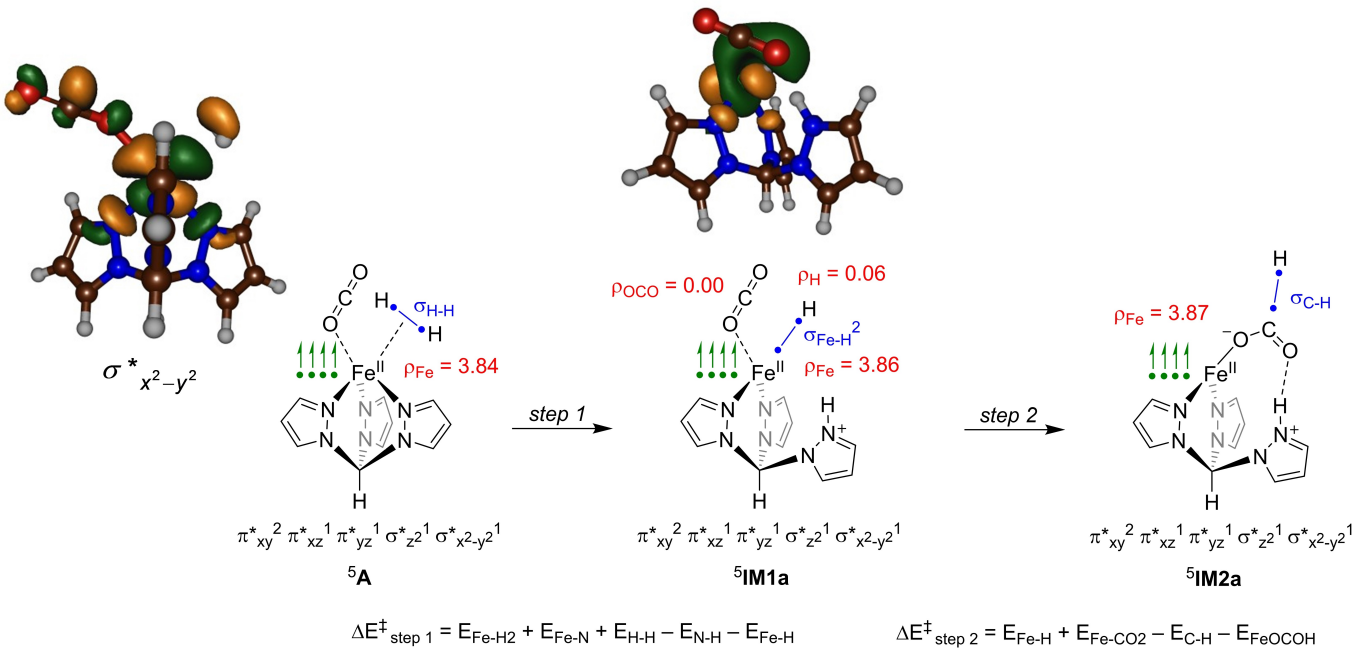

Figure 5. Valence bond description of the first two steps in the reaction mechanism. Unpaired electrons are shown with a dot and arrow (in green), while bonding orbitals are shown as a line between elements with two dots. Group spin densities (ρ) are given in red with values in atomic units. Key valence orbitals are shown.

molecular orbitals and electronic configuration $\pi^*_{xy}{}^2\ \pi^*_{xz}{}^1\ \pi^*_{yz}{}^1\ \sigma^*_{z2}{}^1\ \sigma^*_{x2\text{-}y2}{}^1$. These molecular orbitals represent metal 3d atomic orbitals and their interactions with first-coordination sphere ligands. Thus, the π_{xy}, π_{xz} and π_{yz} orbitals form bonding interactions of the iron $3d_{xy}$, $3d_{xz}$ and $3d_{yz}$ orbitals with 2p orbitals on the nitrogen atoms of the pyrazolyl groups and are all doubly occupied. On the other hand, the antibonding combination of these orbitals, i.e. π^*_{xy}, π^*_{xz} and π^*_{yz} are singly occupied. In addition, there are two σ-type molecular orbitals of relevance, namely σ^*_{z2} and $\sigma^*_{x2\text{-}y2}$. The latter is located in the plane that goes through two pyrazolyl nitrogen atoms, the bound oxygen atom of CO_2 and the H_2 molecule. The orbital is shown on the left-hand-side of Figure 5. As can be seen the H_2 molecular orbital interacts with one of the lobes of the metal $3d_{x2-y2}$ orbital and provides a stable side-on interaction for H_2 binding.

As all first-coordination sphere ligands are weakly bound and neutral, most of the unpaired spin density is on the metal and the valence molecular orbitals are metal-based. In addition, ^{5}**A** binds a H_2 and CO_2 molecule with a H–H of 0.771 Å and C–O distances of 1.171 (inner) and 1.152 (outer) Å. These distances are not significantly longer than those found for isolated H_2 and CO_2 molecules; consequently, they are weakly bound to the iron(II) complex without formation of a covalent bond. Alternative triplet and singlet spin states were also tested but found to be well higher in energy. This is not surprising as trigonal bipyramidal iron(II) complexes generally are in a high-spin state.[19] The iron(II) complex is in a high-spin state with four metal-based unpaired electrons and hence give a large spin density of 3.84 on the iron atom.

The CO_2 hydrogenation reaction starts with heterolytic cleavage of the H–H bond, whereby the two electrons from the H–H bond form the new iron-hydride covalent bond σ_{Fe-H} that is occupied by two electrons. The proton originating from H_2 is transferred to a nitrogen atom of the pyrazole group, which loses its bond to iron and twists away, thereby making space for an Fe–H bond. The hydride electron-pair interacts with the iron $3d_{z2}$ atomic orbital to form a new σ-type bonding orbital, σ_{Fe-H}, shown in Figure 5. Despite the changes in bond topology on iron, the unpaired spin density does not change much and is ρ = 3.86 in ^{5}**IM1a**. Therefore, the four unpaired electrons are assigned to metal-type orbitals in π^*_{xz}, π^*_{yz}, σ^*_{z2} and σ^*_{x2-y2}. Consequently, the electronic configuration and oxidation state on iron have not changed during the H_2 cleavage process. The iron-hydride bond in ^{5}**IM1a** is long, namely 1.703 Å but little spin density is accumulated on the hydride (ρ = 0.06 in ^{5}**IM1a**). Moreover, the charge on the hydride ion is Q = −0.31, which implies a charge-transfer from hydride to iron has taken place through the formation of the covalent Fe–H bond. Therefore, the Fe–H interaction is drawn as a covalent bond (σ_{Fe-H}) with two electrons. The CO_2 group has no unpaired spin density (ρ = 0.0) and consequently no charge-transfer to the CO_2 group has taken place in the process from ^{5}**A** to ^{5}**IM1a**.

We estimated the energy to cleave the H_2 bond in structure ^{5}**A** from the bonds that are broken and formed in the process. Thus, the iron(II)-H_2 bond is broken as well as the heterolytic cleavage of H_2 and both of these interactions are replaced by an iron(II)-hydride interaction. In addition, one of the iron-pyrazolyl bonds breaks and an N–H bond is formed. To estimate the iron(II)-H_2 bond energy (E_{Fe-H2}), we did a single point calculation on the structure of ^{5}**A** with H_2 removed and find a

value of $E_{Fe-H2} = 2.4$ kcal mol^{-1} with respect to ^{5}**A** and H_2. In addition, we did a single point calculation of ^{5}**IM1a** with H_2 removed and its difference in energy with the structure of ^{5}**A** with H_2 removed gives us the strength of the Fe–N bond that is broken (E_{Fe-N}), for which we predict a bond energy of 16.3 kcal mol^{-1}. To estimate the heterolytic cleavage energy of H_2 and the N–H bond that are formed we calculated the reaction of H_2 with water to form hydride and H_3O^+ as a sum of the two values from full geometry optimizations at B3LYP/BS2 level of theory and find $E_{H-H} - E_{N-H} = 87.2$ kcal mol^{-1}. Finally, a single point calculation on ^{5}**IM1a** with the hydride removed was done to estimate the iron(II)-hydride bond energy: $E_{Fe-H} =$ 75.6 kcal mol^{-1}. Based on these estimated bond energies, we predict the heterolytic cleavage of H_2 on the iron(II)-scorpionate complex to be strongly endergonic by 30.4 kcal mol^{-1}. Indeed this step is calculated to be endergonic by close to 20 kcal mol^{-1}, see Figure 2. Therefore, high pressures will be needed to overcome this thermodynamically unfavorable step and push the reaction further into the formate-bound intermediate.

In the next step for cycle 1 the hydride transfer takes place and converts CO_2 into formate into ^{5}**IM2a**. As such the two electrons from the σ_{Fe-H} bond form the new C–H bond orbital σ_{C-H} in formate. At the same time the two π-electrons of one of the C–O bonds in ^{5}**IM1a** become a lone-pair and the formate anion in ^{5}**IM2a**. Energetically, reaction step 2 also includes the replacement of the weakly bound iron(II)-CO_2 interaction into the ionic interaction of iron(II) with formate ion. As such, reaction step 2 will be exergonic and irreversible from ^{5}**IM1a**. This reaction step does not change the spin density on iron and the metal retains four unpaired electrons with a spin density of $\rho = 3.87$ in ^{5}**IM2a** and therefore also the oxidation state of iron does not change. Consequently, the CO_2 hydrogenation is a nucleophilic reaction mechanism rather than a radical reaction type. This is in contrast to aliphatic dehydrogenation reactions by an iron(IV)-oxo complex that proceeds via two successive hydrogen atom abstraction reactions via a radical mechanism.[20]

In summary, the valence bond scheme in Figure 5 shows that the metal acts as a spectator element in the reaction cycle and stays in the iron(II) oxidation state throughout the reaction. However, the metal assists with the H_2 cleavage process and binds donor and acceptor groups and assists with the hydride and proton transfer processes by bringing the donor and acceptor groups close together. In addition, the pyrazolyl groups enable storage of a proton for the final reaction stage leading to products.

Conclusions

In this work a computational study is presented on CO_2 reduction to methanol on an iron(II)-scorpionate catalyst in a reaction with H_2. The calculations show that H_2 and CO_2 bind to the iron(II) center where the reaction takes place in three successive reaction cycles that use one molecule of H_2 each. Each cycle starts with heterolytic cleavage of H_2 into a hydride and a proton, whereby the hydride binds iron(II) and the proton binds to one of the pyrazolyl groups that loses its bond with iron. Thereafter each cycle continues with successive hydride followed by proton transfer to substrate. In cycle one, therefore, CO_2 in converted into formic acid, while in cycle 2 the formic acid is reduced to formaldehyde and water and in the final reaction cycle gives methanol as final product. The calculations give valuable insights into the nature of the catalyst and what drives the reaction. In particular, heterolytic cleavage of H_2 needs to take place, which is an endergonic reaction on the iron(II)-scorpionate system. From a design perspective, the catalysts, therefore, should contain a group that can bind a hydride and a group that can hold a proton prior to reshuttle to substrate. The pyrrole groups of the ligand are excellent sources for the proton relay and even though iron(II) can bind hydride the step is generally endergonic. Moreover, the rate-determining step is hydride transfer to substrate, which particularly is slow for the second cycle and consequently the reaction may stop after formation of formic acid products. The work gives detailed insight on the thermodynamic challenges of using H_2 for CO_2 utilization. In particular, H_2 needs to be cleaved heterolytically and on an iron center that reaction is endergonic. Furthermore, a basic group on the ligand scaffold of the iron is needed to store the proton until it is needed later in the reaction mechanism.

Experimental Section

Density functional theory approaches were used as implemented in the Gaussian-09 software package.[21] The [Fe^{II}(κ^3-HC(pz)$_3$] structure was manually created and one CO_2 and H_2 molecule added to obtain the initial reactant complex. Geometry optimizations, analytical frequencies and constraint geometry scans were performed with the unrestricted B3LYP density functional method in combination with the GD3 dispersion correction with Becke-Johnson damping.[22,23] In addition, all calculations included the self-consistent reaction field approach with a dielectric constant for methanol and an all-electron def2-SVP basis set on all atoms.[24,25] Energies were improved by running a single point calculation with the def2-TZVP basis set on all atoms. Intrinsic reaction coordinate scans were performed from the transition state structures, which confirmed their assignment and what local minima they connect to, see Supporting Information for details. These methods and approaches were validated against experimental rate constants previously and shown to predict free energies of activation by iron complexes to within 3 kcal mol^{-1} and confirm product distributions.[26]

Acknowledgements

The computational shared facilities at the University of Manchester are acknowledged for computational support.

Conflict of Interests

The authors declare no conflict of interest.

Data Availability Statement

The data that support the findings of this study are available in the supplementary material of this article.

Keywords: density functional theory · inorganic reaction mechanisms · CO_2 reduction · iron · homogeneous catalysis

[1] a) M. Aresta, A. Dibenedetto, E. Quaranta, *J. Catal.* **2016**, *343*, 2–45; b) M. He, Y. Sun, B. Han, *Angew. Chem. Int. Ed.* **2013**, *52*, 9620–9633; c) R. Francke, B. Schille, M. Roemelt, *Chem. Rev.* **2018**, *118*, 4631–4701; d) B. S. Crandall, S. Overa, H. Shin, F. Jiao, *Acc. Chem. Res.* **2023**, *56*, 1505–1516.
[2] a) J. Shi, Y. Jiang, Z. Jiang, X. Wang, X. Wang, S. Zhang, P. Han, C. Yang, *Chem. Soc. Rev.* **2015**, *44*, 5981–6000; b) T. Wagner, U. Ermler, S. Shima, *Science* **2016**, *354*, 114–117; c) M. Roger, F. Brown, W. Gabrielli, F. Sargent, *Curr. Biol.* **2018**, *28*, 140–145; d) S. Bierbaumer, M. Nattermann, L. Schulz, R. Zschoche, T. J. Erb, C. K. Winkler, M. Tinzl, S. M. Glueck, *Chem. Rev.* **2023**, *123*, 5702–5754.
[3] a) A. Ogawa, K. Oohora, W. Gua, T. Hayashi, *Chem. Commun.* **2018**, *55*, 493–496; b) S. Fukuzumi, Y.-M. Lee, H. S. Ahn, W. Nam, *Chem. Sci.* **2018**, *9*, 6017–6034; c) S. Chatterjee, K. Sengupta, B. Mondal, S. Dey, A. Dey, *Acc. Chem. Res.* **2017**, *50*, 1744–1753; d) H. Rao, J. Bonin, M. Robert, *J. Phys. Chem. C* **2018**, *122*, 13834–13839; e) F. Franco, M. F. Pinto, B. Royo, J. Lloret-Fillol, *Angew. Chem. Int. Ed.* **2018**, *57*, 4693–4696; f) X.-F. Liu, X.-Y. Li, L.-N. He, *Eur. J. Org. Chem.* **2019**, *2019*, 2437–2447; g) S. Fernández, F. Franco, M. Martínez Belmonte, S. Friães, B. Royo, J. M. Luis, J. Lloret-Fillol, *ACS Catal.* **2023**, *13*, 10375–10385.
[4] a) C. Costentin, G. Passard, M. Robert, J.-M. Savéant, *Proc. Natl. Acad. Sci. USA* **2014**, *111*, 14990–14994; b) A. Maurin, M. Robert, *J. Am. Chem. Soc.* **2016**, *138*, 2492–2495; c) J. S. Derrick, M. Loipersberger, R. Chatterjee, D. A. Iovan, P. T. Smith, K. Chakarawet, J. Yano, J. R. Long, M. Head-Gordon, C. J. Chang, *J. Am. Chem. Soc.* **2020**, *142*, 20489–20501; d) M. Abdinejad, C. Dao, X.-A. Zhang, H. B. Kraatz, *J. Energy Chem.* **2021**, *58*, 162–169; e) C. Zhang, D. Dragoe, F. Brisset, B. Boitrel, B. Lassalle-Kaiser, W. Leibl, Z. Halime, A. Aukauloo, *Green Chem.* **2021**, *23*, 8979–8987; f) N. Devi, C. K. Williams, A. Chaturvedi, J. Jiang, *ACS Appl. Energ. Mater.* **2021**, *4*, 3604–3611; g) J. S. Derrick, M. Loipersberger, S. K. Nistanaki, A. V. Rothweiler, M. Head-Gordon, E. M. Nichols, C. J. Chang, *J. Am. Chem. Soc.* **2022**, *144*, 11656–11663; h) D. Mendoza, S.-T. Dong, N. Kostopoulos, V. Pinty, O. Rivada-Wheelaghan, E. Anxolabéhère-Mallart, M. Robert, B. Lassalle-Kaiser, *ChemCatChem.* **2023**, *15*, e202201298.
[5] a) P. Davethu, S. P. de Visser, *J. Phys. Chem. A* **2019**, *123*, 6527–6535; b) M. Tarrago, S. Ye, F. Neese, *Chem. Sci.* **2022**, *13*, 10029–10047; c) R. Khakpour, K. Laasonen, M. Busch, *Electrochim. Acta* **2023**, *442*, 141784.
[6] M. Abdinejad, C. Dao, B. Deng, F. Dinic, O. Voznyy, X.-a. Zhang, H.-B. Kraatz, *ACS Sustainable Chem. Eng.* **2020**, *8*, 1715–1720.
[7] M. Montandon-Clerc, G. Laurenczy, *J. Catal.* **2018**, *362*, 78–84.
[8] E. M. Lane, Y. Zhang, N. Hazari, W. H. Bernskoetter, *Organometallics* **2019**, *38*, 3084–3091.
[9] S. Kar, A. Goeppert, J. Kothandaraman, G. K. S. Prakash, *ACS Catal.* **2017**, *7*, 6347–6351.
[10] A. P. C. Ribeiro, L. M. D. R. S. Martins, A. J. L. Pombeiro, *Green Chem.* **2017**, *19*, 4811–4815.
[11] S. Carlotto, G. Casella, L. Floreano, A. Verdini, A. P. C. Ribeiro, L. M. D. R. S. Martins, M. Casarin, *Catal. Today* **2020**, *358*, 403–411.
[12] See, e.g., a) S. Shaik, D. Kumar, S. P. de Visser, A. Altun, W. Thiel, *Chem. Rev.* **2005**, *105*, 2279–2328; b) S. P. de Visser, Y.-T. Lin, H. S. Ali, U. K. Bagha, G. Mukherjee, C. V. Sastri, *Coord. Chem. Rev.* **2021**, *439*, 213914; c) S. P. de Visser, G. Mukherjee, H. S. Ali, C. V. Sastri, *Acc. Chem. Res.* **2022**, *55*, 65–74.
[13] a) X. Yang, *ACS Catal.* **2011**, *1*, 849–854; b) C. Dong, M. Ji, X. Yang, J. Yao, H. Chen, *Catalysts* **2017**, *7*, 5; c) X. Yan, H. Ge, X. Yang, *Inorg. Chem.* **2019**, *58*, 5494–5502; d) M. Loipersberger, D. G. A. Cabral, D. B. K. Chu, M. Head-Gordon, *J. Am. Chem. Soc.* **2021**, *143*, 744–763; e) M. Loipersberger, J. S. Derrick, C. J. Chang, M. Head-Gordon, *Inorg. Chem.* **2022**, *61*, 6919–6933.
[14] a) H. M. Berman, J. Westbrook, Z. Feng, G. Gilliland, T. N. Bhat, H. Weissig, I. N. Shindyalov, P. E. Bourne, *Nucl. Acids Res.* **2000**, *28*, 235–242; b) S. Ghafoor, A. Mansha, S. P. de Visser, *J. Am. Chem. Soc.* **2019**, *141*, 20278–20292; c) X. Sheng, M. Kazemi, F. Planas, F. Himo, *ACS Catal.* **2020**, *10*, 6430–6449; d) Z. Wojdyla, T. Borowski, *Chem. Eur. J.* **2022**, *28*, e202104106; e) Y.-T. Lin, H. S. Ali, S. P. de Visser, *Chem. Eur. J.* **2022**, *28*, e202103982.
[15] a) H. Fong, J. C. Peters, *Inorg. Chem.* **2015**, *54*, 5124–5135; b) J. E. Vandezande, H. F. Schaefer III, *Organometallics* **2018**, *37*, 337–342.
[16] a) F. G. Cantú Reinhard, P. Barman, G. Mukherjee, J. Kumar, D. Kumar, D. Kumar, C. V. Sastri, S. P. de Visser, *J. Am. Chem. Soc.* **2017**, *139*, 18328–18338; b) G. Mukherjee, A. Alili, P. Barman, D. Kumar, C. V. Sastri, S. P. de Visser, *Chem. Eur. J.* **2019**, *25*, 5086–5098; c) P. Barman, F. G. Cantú Reinhard, U. K. Bagha, D. Kumar, C. V. Sastri, S. P. de Visser, *Angew. Chem. Int. Ed.* **2019**, *58*, 10639–10643.
[17] a) S. Shaik, D. Kumar, S. P. de Visser, *J. Am. Chem. Soc.* **2008**, *130*, 10128–10140; b) D. Li, Y. Wang, K. Han, *Coord. Chem. Rev.* **2012**, *256*, 1137–1150; c) S. Kalita, S. Shaik, K. D. Dubey, *Chem. Sci.* **2021**, *12*, 14507–14518; d) G. Mukherjee, J. K. Satpathy, U. K. Bagha, M. Q. E. Mubarak, C. V. Sastri, S. P. de Visser, *ACS Catal.* **2021**, *11*, 9761–9797.
[18] a) C. Colomban, A. H. Tobing, G. Mukherjee, C. V. Sastri, A. B. Sorokin, S. P. de Visser, *Chem. Eur. J.* **2019**, *25*, 14320–14331; b) S. Louka, S. M. Barry, D. J. Heyes, M. Q. E. Mubarak, H. S. Ali, L. M. Alkhalaf, A. W. Munro, N. S. Scrutton, G. L. Challis, S. P. de Visser, *J. Am. Chem. Soc.* **2020**, *142*, 15764–15779; c) E. F. Gérard, V. Yadav, D. P. Goldberg, S. P. de Visser, *J. Am. Chem. Soc.* **2022**, *144*, 10752–10767.
[19] a) R. Latifi, M. A. Sainna, E. V. Rybak-Akimova, S. P. de Visser, *Chem. Eur. J.* **2013**, *19*, 4058–4068; b) C.-C. G. Yeh, C. Pierides, G. N. L. Jameson, S. P. de Visser, *Chem. Eur. J.* **2021**, *27*, 13793–13806; c) C.-C. G. Yeh, S. Ghafoor, J. K. Satpathy, T. Mokkawes, C. V. Sastri, S. P. de Visser, *ACS Catal.* **2022**, *12*, 3923–3937.
[20] a) L. Ji, A. S. Faponle, M. G. Quesne, M. A. Sainna, J. Zhang, A. Franke, D. Kumar, R. van Eldik, W. Liu, S. P. de Visser, *Chem. Eur. J.* **2015**, *21*, 9083–9092; b) H. S. Ali, R. H. Henchman, S. P. de Visser, *ChemCatChem.* **2021**, *13*, 3054–3066; c) H. S. Ali, J. Warwicker, S. P. de Visser, *ACS Catal.* **2023**, *13*, 10705–10721.
[21] *Gaussian-09, Revision D.01*, M. J. Frisch, G. W. Trucks, H. B. Schlegel, G. E. Scuseria, M. A. Robb, J. R. Cheeseman, G. Scalmani, V. Barone, B. Mennucci, G. A. Petersson, H. Nakatsuji, M. Caricato, X. Li, H. P. Hratchian, A. F. Izmaylov, J. Bloino, G. Zheng, J. L. Sonnenberg, M. Hada, M. Ehara, K. Toyota, R. Fukuda, J. Hasegawa, M. Ishida, T. Nakajima, Y. Honda, O. Kitao, H. Nakai, T. Vreven, J. A. Montgomery Jr., J. E. Peralta, F. Ogliaro, M. Bearpark, J. J. Heyd, E. Brothers, K. N. Kudin, V. N. Staroverov, T. Keith, R. Kobayashi, J. Normand, K. Raghavachari, A. Rendell, J. C. Burant, S. S. Iyengar, J. Tomasi, M. Cossi, N. Rega, J. M. Millam, M. Klene, J. E. Knox, J. B. Cross, V. Bakken, C. Adamo, J. Jaramillo, R. Gomperts, R. E. Stratmann, O. Yazyev, A. J. Austin, R. Cammi, C. Pomelli, J. W. Ochterski, R. L. Martin, K. Morokuma, V. G. Zakrzewski, G. A. Voth, P. Salvador, J. J. Dannenberg, S. Dapprich, A. D. Daniels, O. Farkas, J. B. Foresman, J. V. Ortiz, J. Cioslowski, D. J. Fox, Gaussian, Inc., Wallingford CT **2010**.
[22] a) A. D. Becke, *J. Chem. Phys.* **1993**, *98*, 5648–5652; b) C. Lee, W. Yang, R. G. Parr, *Phys. Rev. B* **1988**, *37*, 785–789.
[23] S. Grimme, S. Ehrlich, L. Goerigk, *J. Comb. Chem.* **2011**, *32*, 1456–1465.
[24] J. Tomasi, B. Mennucci, R. Cammi, *Chem. Rev.* **2005**, *105*, 2999–3094.
[25] A. Schaefer, H. Horn, R. Ahlrichs, *J. Chem. Phys.* **1992**, *97*, 2571–2577.
[26] a) H. S. Ali, S. P. de Visser, *Chem. Eur. J.* **2022**, *28*, e202104167 ; b) T. Mokkawes, S. P. de Visser, *Chem. Eur. J.* **2023**, *29*, e202203875; c) U. K. Bagha, R. Yadav, T. Mokkawes, J. K. Satpathy, D. Kumar, C. V. Sastri, S. P. de Visser, *Chem. Eur. J.* **2023**, *29*, e202300478.

Manuscript received: September 7, 2023
Accepted manuscript online: September 11, 2023
Version of record online: ■■, ■■

RESEARCH ARTICLE

CO_2 to methanol: Density functional theory calculations on the mechanism of the reduction of CO_2 by H_2 on an iron(II) center show the reaction to proceed through heterolytic cleavage of H_2, whereby the ligand holds the proton during the reaction.

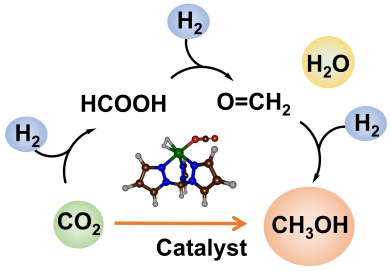

*C. Zhu, Dr. C. D'Agostino, Dr. S. P. de Visser**

1 – 12

Mechanism of CO_2 Reduction to Methanol with H_2 on an Iron(II)-scorpionate Catalyst